Improved model and experimental validation of deformation in fused filament fabrication of polylactic acid

Bas Wijnen, Paul Sanders, Joshua Pearce

Improved Model and Experimental Validation of Deformation in Fused Filament Fabrication of Poly Lactic Acid

Bas Wijnen [1] Paul Sanders [1] and Joshua M. Pearce [1,2,*]
1 Department of Materials Science & Engineering, Michigan Technological University
2 Department of Electrical & Computer Engineering, Michigan Technological University
* Corresponding author
1400 Townsend Drive
Houghton, MI 49931-1295
pearce@mtu.edu

Abstract

RepRaps (self Replicating Rapid prototypers), which 3-D print objects using fused filament fabrication (FFF), have evolved rapidly since their open source introduction. These 3-D printers have primarily been limited to desktop sizes of volumes of ~8000 cm³, which has limited the attention of the scientific community to investigating deformation of common thermoplastics such as polylactic acid (PLA) used in FFF printing. The only existing physically relevant deformation model was expanded here to use a physics-based temperature gradient instead of a step function. This was necessary to generalize the model to 3-D printing in a room temperature environment without a heated chamber. The thermal equation was calibrated using thermal measurements and validated by measuring curvatures in printed objects. The results confirm that this is a valid model for predicting warpage of thin vertical walls of PLA. Additionally, the effect of annealing was examined. It was found that at a temperature of 50°C, no shrinkage or crystallization takes place, but at 90°C the PLA rapidly crystallizes to around 20% crystallinity. This indicates that heated bed temperatures should be maintained at 50ºC or lower to avoid print failure (premature substrate release) with PLA. At 90°C, the annealing is accompanied by a 5% size decrease in both horizontal dimensions, but an 8% increase in the vertical dimension. Thus, the volume decreased by only 3%. This observation may lead to potential methods of improving slicing of printing large PLA objects with FFF.

Keywords

Fused filament fabrication; fused deposition modeling; deformation; 3-D printing; poly lactic acid; RepRap

Acknowledgments

Conflict of Interest: The authors have no conflicts of interest.

1. Introduction

RepRaps (self Replicating Rapid prototypers) which 3-D print objects using fused filament fabrication (FFF) have evolved rapidly since their open source introduction [1-3]. There are now dozens of RepRap designs [4] and the majority of the prosumer 3-D printers on the market are derived from RepRaps [5] including *Make* magazine's best 3-D printer of 2015 the open source Lulzbot Taz [6] and the best 3-D printer for 2016 the open source Prusa I3 [7]. With this rapid technological evolution, FFF 3-D printing applications have also exploded and have opened many doors for applications that were previously only affordable for large companies such as: open source appropriate technology for sustainable development [8-11], personal fabrication [12], small custom print shops [13], scientific equipment [14-22], microfluidics [23], solar photovoltaic racking [24,25], dentistry [26,27], medicine [28-31]; farming equipment [32], education [33-39], and museum replications [40].

So far, the new FFF 3-D printers have mostly been limited to desktop sized models, which primarily print in poly lactic acid (PLA) with a thermal coefficient of linear expansion α of $8.5 \cdot 10^{-5}$ K^{-1}[41] because it demonstrates less warping during a print than other materials such as ABS (α up to $15 \cdot 10^{-5}$ K^{-1} [41]) or HDPE (α up to $11 \cdot 10^{-5}$ K^{-1} [41]) plastic and the emissions during printing are less dangerous [42]. Furthermore, PLA is made from corn-based resin, making it non-toxic, biodegradable, and able to be produced in environmentally friendly, renewable processes [43,44]. The size of the printers (around 8,000 cm³) have limited the size of the prints that can be made with them. There have, however, also been attempts to use larger machines as open source hardware 3-D printers such as the Gigabot (212,400 cm³) developed by

re:3D [45].

Because of the limited adoption, not much attention has been given so far to the challenges that large scale FFF 3-D printing presents. The main challenge is to limit the deformation of the printed part during the printing process. To obtain deformation-free high-quality prototypes remains one of the most important challenges in the rapid prototyping field [46] as a whole and the additive manufacturing field in particular. Due to temperature gradients in the print, the edges tend to warp upwards as seen in Figure 1. The effect scales with the size of the printed object, so with larger prints, it is a larger absolute deformation. If the effect is too large, the object will release from the substrate before it is completed, and the print will have failed. Residual stress [47] and crystallinity [48] are important parameters for the properties of printed objects and the determination of deformation, however the deformation process of FFF is not well understood.
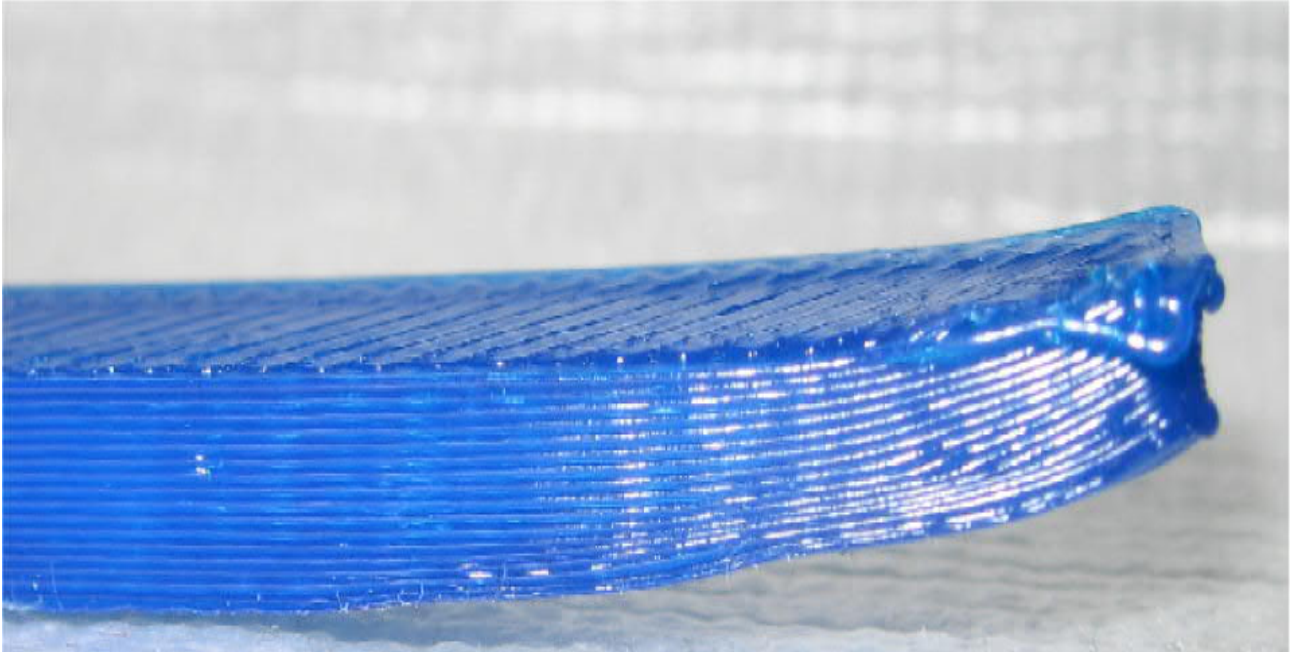

Figure 1: Commonly observed deformation in the first layers of 3-D printed PLA. Scale bar: 1 cm.

This study presents theory and experiments to investigate the mechanisms behind the deformation in PLA during FFF. First, existing models and their deficiencies in producing a remedy for deformation in 3-D printing PLA are reviewed. A 1-dimensional model is expanded to use a physics based temperature gradient, and it is verified using a measured temperature gradient in a printed part. The changes in size and crystallinity before and after annealing are measured to explain substrate release several hours into the print.

2. Background
2.1 Models of Deformation in FFF

Some very limited research has been done to prevent deformation in fused filament fabrication (and the subclass of fused deposition modeling, FDM). For plastic parts, a model was proposed to explain warpage [49] and tested on an FDM printer for number of layers, layer height and chamber temperature of an enclosed proprietary printer. This model uses a heated build chamber, so the temperature gradients were smaller. Because of this, it assumes that the gradient is a step function, where only the newly printed layer is not cooled to the chamber temperature yet. It thus simulates detaching a newly printed layer letting it cool to the chamber temperature and then straining that layer back to the original length, reattaching it and enforcing equilibrium conditions. Although this is non-physical it provides useful results particularly for the class of printer for which it was targeted. Based on this model, an alternative method for toolpath creation has been proposed and demonstrated to limit warpage of the printed object [50]. This method limits the length of the traces by dividing the object into bricks. Their results show that this limits the warpage, as predicted by the model.

A second model was developed by Xinhua et al. [51]. This model also simplifies the temperature gradient in the object that is being printed as a step function, and assumes every layer to be deposited in zero time [51]. It is based on a model for deformation of a thin plate with a vertical load [52]. This does not correspond to the modeled scenario, and

therefore it does not give relevant results. It is unclear how the final deformation is computed from the given formula. The system only varies in the vertical direction, and the model that was used predicts zero deformation for that case. Xinhua et al. then continue to determine optimal process parameters for thin plates based on experiments, but the model's predictions are not compared to the experimental results [51] and continuation of this model is not recommended.

Thus in this study, Wang et al.'s model is extended to a physics-based generalizable system of FFF without a heated chamber.

2.2 PLA and FFF

PLA is a thermoplastic polymer that is produced from natural sources such as corn. Its chemical formula is $(C_3H_4O_2)_n$. It is nontoxic and biodegradable, making it a popular choice for packaging and 3-D printing. Another feature that makes it good for 3-D printing is its limited shrinkage compared to other thermoplastics such as ABS.

Polymers can have varying degrees of crystallinity and PLA is no exception. Crystallinity of commercial PLA filament varies due in part to coloring agents [48]. Annealing causes PLA to crystallize, following standard Avrami crystallization kinetics [53]. Like other polymers, PLA can also be crystallized by stretching it while it is below the melting temperature, but above the glass transition temperature.

The PLA molecule is chiral, so there are two isomers of it, PLLA and PDLA. Pure forms of either of the isomers more easily crystallize, but the mixture has a higher melting point [54]. The density of amorphous PLLA is 1248 kg/m^3, while for crystalline PLLA it is 1290 kg/m^3, so there is a volume decrease of 3.3%. Crystallization of PLA takes place around nucleation sites in the form of spherulites: spherical structures of outward extending arms [53,54]. The glass transition temperature and melting temperature of PLA depend on the mixture of PLLA and PLDA and on the crystallinity. The glass transition temperature of semi-crystalline PLA is around 58°C and the melting temperature is between 130°C and 230°C [55].

During FFF 3-D printing, the PLA is first heated to a temperature near the melting temperature (T_m) but above the glass transition temperature (T_g). It is then extruded and deposited on the object that is being printed in the temperature range between T_m and T_g. During this time PLA can acquire a large deformation with less force and the strength is small [56]. The object cools as the print progresses and internal stress is accumulated [49]. The substrate may be heated, resulting in an even more complex temperature gradient in the object. Heating a chamber in which the 3-D printer is placed [57,58] or a printer with an integrated heated build chamber such as the GolemD [59] or the Kühling&Kühling RepRap Industrial 3-D printer [60], on the other hand, keeps the differences smaller. Most proprietary 3-D printers have enclosed heated build chambers, which helps them limit the warpage.

The extrusion causes the material to decrystallize [61]. This effect is stronger at a lower temperature. The cooling leads to shrinkage, and because of the temperature gradient, this leads to internal stress and deformation. Finally, a heated substrate may anneal the lower layers of the object, and a heated chamber may anneal the entire object. This results in crystallization of the PLA. All of these processes will be probed to develop a full model.

3. Methods
3.1 Materials
All objects were printed from PLA that was extruded from resin (Natureworks 4043D 25kg polylactide resin) without additives [62]. Some properties of this material are summarized in Table 1.

Table 1: Selected properties of the polymer that was used during the experiments.

Glass transition temperature (T_g)	~58°C
Melting temperature (T_m)	130-230°C
Linear coefficient of thermal expansion	~$8.5 \cdot 10^{-5}$ K^{-1}
Diameter before extrusion	1.75 mm
Diameter of extrusion nozzle	0.5 mm
Density	1248-1290 kg/m^3
Poisson's ratio	0.36

3.2 3-D Printing
The prints were made on a MOST RepRap 3-D printer [63], with a 0.5 mm nozzle. The substrate was regular soda-lime glass without heating. The substrate was cleaned with soap and distilled water and dried with compressed air. While application of glue to the substrate improves bed adhesion, it can interfere with x-ray diffraction (XRD) measurements and

was avoided.

For all experiments, the 3-D printer was controlled using Franklin [64]. The objects that were measured with XRD were created with OpenSCAD [66] and sliced using Slic3r [67] with 100% infill. The infill was set to be lines that are parallel to the sides of the object, alternating between the long and the short direction. The toolpath for the temperature measurement was created using a custom Python script [68].

3.4 Measurements
3.4.1 Temperature

Temperature graphs of a thin vertical wall were made while printing using an infrared sensitive camera (FLIR e60). The recordings were stored as mp4 movie files by the camera, in false color with a scale bar on screen. Also included on screen was the temperature of the center of the image. Figure 4 is a frame from one recording.

The temperature of the pixels on the image was determined from the image. The red, green and blue channels of the pixels in the scale bar were plotted against their position in the scale bar. The plot was divided into regions where at least one component had a linear dependence on temperature. Those linear relations were manually fit in order to convert a pixel's color value into a position on the scale. Because the upper and lower limits of the scale varied, and those variations were not updated immediately in the image, they also had to be determined from the image. The constant temperature background was used as a reference. The reported temperature of the central pixel was updated immediately, and was used as the second reference. The two references were used to convert the position on the scale into a temperature. Some images were not scaled correctly and those were omitted from the analysis.

The vertical temperature gradient of a thin vertical wall was examined while it was being printed. The toolpath started with a line next to the wall to prime the extruder. Then the nozzle retracted and moved to a parking position behind the wall. It then moved to the middle of the wall, unretracted while it moved to the left side, extruded a line of filament while moving to the right, then another line just behind it while going back to the left. Then it moved back to the center while retracting, followed by a move back to the parking position. The move to the center ensured that the wall was not pulled sideways. This was important because it was printed on bare glass, and would be pulled off the substrate otherwise. After this, the same procedure was repeated for the next layer, with left and right reversed. Layers were added similarly until the top of the object was reached. The images that were used for analysis were always every second layer, with the extruder in the same position and moving in the same direction.

3.4.2 Temperature Model

To enable extension and improvement of Wang et al.'s work to a more generalizable FFF 3-D printing scenario a physics-based model for the temperature gradient in the printed object was derived. The existing model uses a step function for the temperature. This is a simplification that is only valid if the environment temperature is relatively high. The improvement in this work was to replace the step function with a physics-based temperature gradient that was fit to a set of measured temperatures.

The change in temperature with time has three components. Conductivity is proportional to the second derivative of the temperature to the position, convection is proportional to the temperature difference between the object and the air, and radiation is proportional to the fourth power of the absolute temperature of the object. There is also incoming radiation, which is proportional to the fourth power of the absolute environment temperature.

The model assumes symmetry in both horizontal directions, so z is the only spatial variable of interest:

$$\frac{\partial T}{\partial t} = C_0 \frac{\partial^2 T}{\partial z^2} - C_1 \Delta T - \sigma \Delta \left(T^4 \right)$$

(1)

In this equation, C_0 and C_1 are proportionality constants for conduction and convection respectively, and σ is the Stefan-Boltzmann constant.

This equation does not have an analytical solution. Therefore, it was simplified to ignore radiation. This simplification is justified for temperatures close to the environment temperature, where conduction and convection are much more important factors for heat transport than radiation. For FFF 3-D printing, this is applicable. For an object of 200°C in an environment of 20°C, radiation accounts for a heat loss of only 10 μW/m^2.

3-D printing is modeled as a continuous process. The top of the object grows with time at a speed v. The temperature difference between the top boundary and the air is always T□. With this simplification and boundary condition, the solution to the equation is:

4

$$\Delta T\left(z,t\right)=T_0\, e^{\frac{a}{v}z-at} \tag{2}$$

In this solution, a is a function of $C\square$, $C\square$ and v. Because $C\square$ depends on many properties, including ambient temperature, air flow and humidity, no attempt is made to predict its value, and instead a is fit to the measurement. The only time of interest is at the end of the print, so t=h/v.

The temperature gradient above (Equation 2) was applied instead of the step function in Wang's model instead of the step function that was used there (where ΔT is T_g-T_e when s≤z≤h and 0 when 0≤z≤s). The other two equations remain identical:

$$\int_0^h \left(-E\alpha\Delta T+\sigma'+\frac{Ez}{R}\right)dz=0 \tag{3}$$

$$\int_0^h \left(-E\alpha\Delta T+\sigma'+\frac{Ez}{R}\right)z\,dz=0 \tag{4}$$

In these equations, E is the elastic modules which is 1.03 GPa for amorphous PLA [53], and α is the linear shrinkage coefficient, which is $8.5\cdot10^{-}\square K^{-1}$ [41]. σ' is a combination of several stress components, which is simplified in the original model by treating it as a scalar. Finally, h is the height of the object. This simplification is used in this improved model as well.

Equations 2, 3 and 4 can be solved for the curvature k=1/R:

$$k\left(h\right)=\frac{6\alpha T_0}{h^2}\left(2+\frac{2v^2-a^2h}{ahv}\left(e^{-\frac{h}{v}a}-1\right)\right) \tag{5}$$

To verify this model, a wall was printed as in the temperature measurement, and it was broken off the substrate immediately after completion of the print, and left to cool to room temperature normally. It should be noted that there is a difference between this method and what is modeled. The substrate is not part of the model, and therefore the predictions for layers closer to the substrate are unreliable, because the thermal conductivity and heat capacity of the substrate differ from a continuing wall of PLA. For high objects, this introduces a small error, while for low objects, the error will be larger, because the layers of those objects are on average closer to the substrate.

The resulting warped objects were scanned at 600 dpi on a flat bed scanner and the scans were analyzed using Gimp [69] using its measurement tool to measure distances and angles in the image. The height of the object (h) was verified to be what it was printed as, and the distance from the line between the two tips of the object to the lowest point on the top layer, in the middle (δ), was measured by first rotating the image to make this line vertical, and then using the rectangular select tool to measure the horizontal distance. This is the amount of warp. From this and the length of the object, the radius of curvature (R) was computed and compared to the predicted value. A diagram with the variables is shown in Figure 2.

3.4.3 Crystallinity

Rectangular blocks of 10cm×2.8cm×1cm were printed on bare glass as shown in Figure 3 and annealed at 50°C using an electric heater between 0 and 4 hours. This temperature is just below the glass transition temperature of approximately 58°C and was chosen as representative for a typical heated substrate during a print. The size before and after annealing was measured, and crystallinity was measured using XRD with a Scintag XDS 2000 theta-theta powder diffractometer with a copper X-ray tube, 1 mm and 2 mm beam slits and 0.3 mm and 0.5 mm receiving slits and a graphite monochromator. The printed block was placed in the sample holder with the smooth bottom layer facing the instrument. The X-ray source and the detector were moved simultaneously and the intensity of the reflection was measured at each angle. Crystallinity was determined by dividing the area of the crystalline peaks by the total area of the measurement.
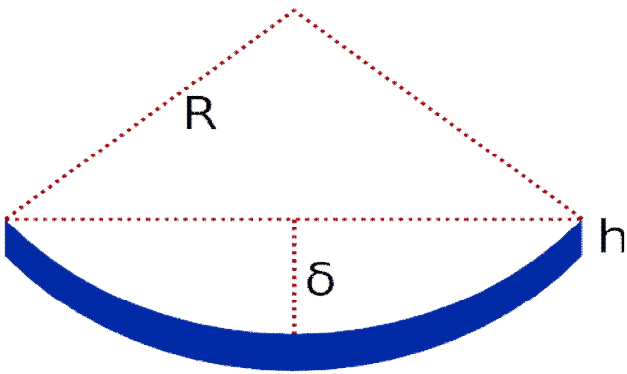
Figure 2: Schematic showing the meaning of the variables in an exaggerated example of warping.
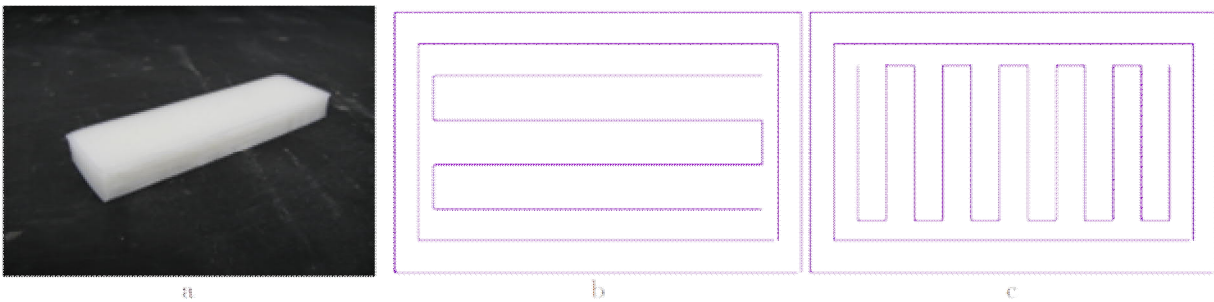

Figure 3: Samples that were used for the XRD measurements. a) Photograph of the sample, dimensions are 10×2.8×1 cm. b) Diagram of the print path for odd layers. c) Diagram of the print path for even layers. The number of lines in the diagrams of the print paths has been reduced for clarity.

The parts are expected to crystallize during annealing, and shrink as a result of that. Because no crystallinity was observed even as a result of 4 hours of annealing, the blocks were annealed again for the same time as before, but now at 90°C. The size and crystallinity were determined again after this.

In order to better understand the deformation during annealing, the object that was not annealed and the one that was annealed for 1 hour at both temperatures were frozen with liquid nitrogen and broken with a pair of pliers while holding them in a vise. The parts were left to warm up to room temperature and for both samples the interface was inspected with an FEI XL-40 environmental scanning electron microscope (ESEM), using the backscatter electron detector, 10 kV accelerating voltage and a working distance of 10 mm. The FESEM images were analyzed using a pixel count in the GNU Image Manipulation Program [69].

4. Results

4.1 Temperature and Deformation

An example frame that was used for one curve is shown in Figure 4 with the hotend moving to the right. As can be seen in Figure 4, the clean glass substrate is highly reflective at the large angle and these reflections were not analyzed. It is also clear that the hottest PLA has just left the nozzle and the coldest PLA is on the bottom layer on the return side, which has had the longest to cool. There is a clear temperature gradient from the substrate surface to the print surface. The emissivity of the PLA is high at 0.95. This is good for the precision of the measurement. Figure 5 shows the gradient of the temperature in the vertical wall in steps of two layers. Every curve had the print head in the same position and moving in the same direction. The curves become longer as the print becomes taller. The maximum intensity is the most recently printed layer. The thermal model was fit to the data and is shown in Figure 5 as smooth lines. The lines deviate significantly from the measured temperatures. The model assumes a continuous growth of the top, while in reality it is built in layers. The top is kept at a constant temperature in the model. The average temperature of the top layer in reality depends on the cooling rate. Insofar as the model is correct, the height at which the average is constant may not be exactly at the top of the print. This could have been included in the model as an extra parameter. However, doing this led to the model becoming unstable,
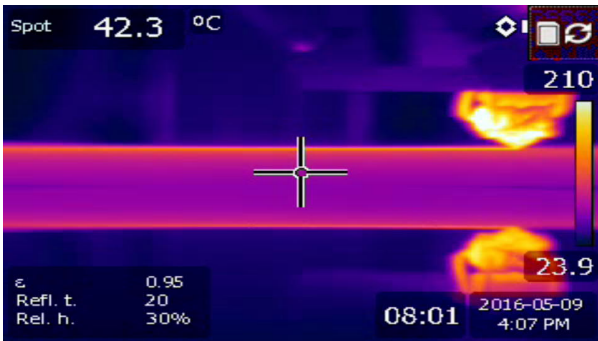
due to too many parameters.

Figure 4: A representative infrared image that was used to measure the temperature of the printed object. The bright object is the nozzle, which is moving towards the right. The bright line is the most recently printed layer. The mirrored image on the lower side is the reflection in the glass substrate. The reported spot temperature of 42.3°C is in the center of the cross.

The data drops more steeply than the model at the higher temperatures. This causes the base of the fit to be higher than the data. This means that the model predicts the curves to be closer to the environment temperature than they actually are, while the environment temperature is fit to a higher value than it actually is. The fit found an environment temperature of 45°C while it was around 20°C in reality, and an average top layer temperature of 74°C. The actual value of the top layer temperature can be seen in the graph. The value of a, the parameter that combines several constants, was fit to 0.012 s^{-1}. The high environment temperature is explained by the design of the 3-D printer, which blows air past the extruder and onto the object. This air is warmed up by the extruder, and therefore the environmental air of the object during printing is higher than room temperature.
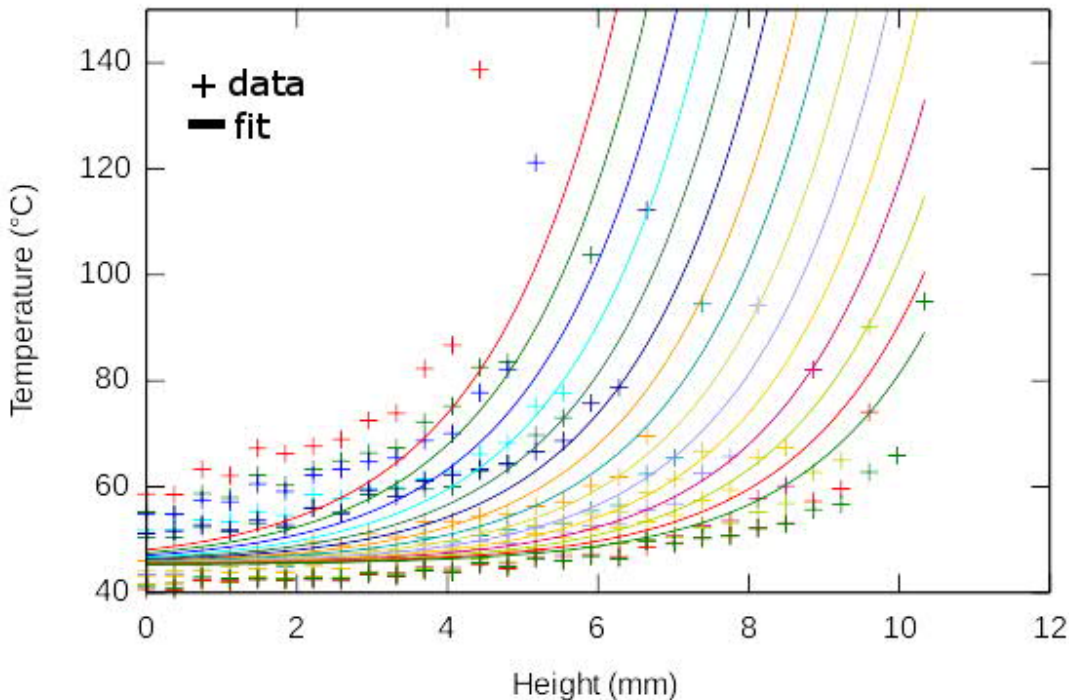

Figure 5: Vertical gradient of the temperature at several points in time. The curves are the fit of the thermal model to the data.

4.2 Microstructure and Deformation

7

Before annealing, but also after annealing the objects at 50°C, no crystalline peaks were visible on the XRD spectra. The XRD spectrum for the sample that was annealed for 4 hours at 50°C, and the spectrum for the sample that was annealed for two hours at 50°C and then 2 hours at 90°C are shown in Figure 6. As can be seen, the sample annealed at 50°C is completely amorphous, while the sample annealed at 90°C clearly shows crystallinity. To determine the crystallinity, it was first determined that three broad Pearson 7 peaks fit the amorphous spectrum well. Then in the spectra with crystalline peaks, the amorphous background was fit to three broad peaks as well. The total area under the crystalline peaks was divided by the total area of all peaks to determine the crystallinity of the sample.

After annealing for 1 hour at 90°C, the crystallinity was almost 20%, and further annealing did not make it go up much further (Figure 7).
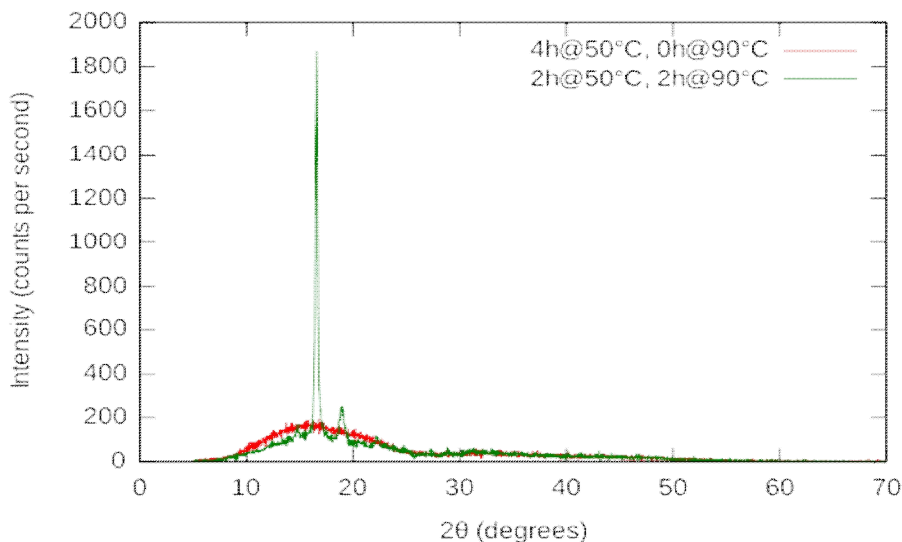

Figure 6: XRD spectra for the sample that was only annealed at 50°C, and the sample that was first annealed for two hours at 50°C, then for two hours at 90°C.
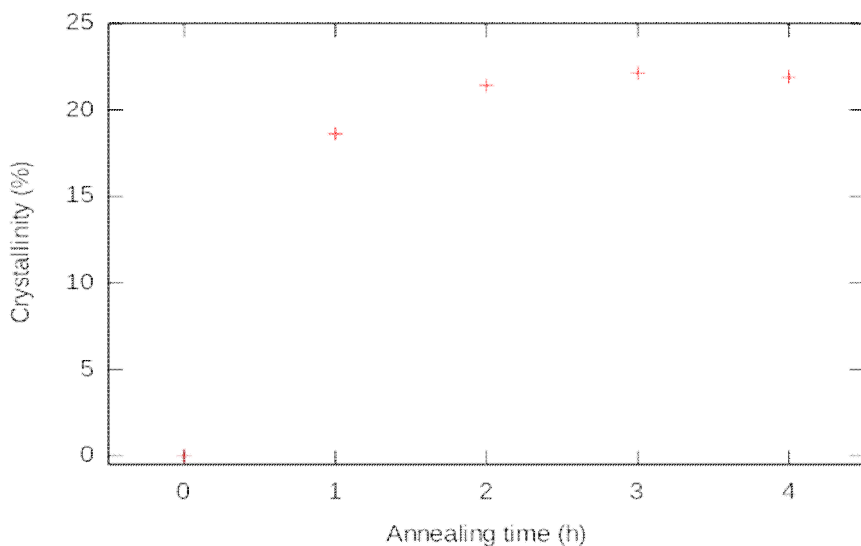

Figure 7: Crystallinity as a function of annealing time when annealing at 90°C.

The size of the objects is shown in Figure 8. The absence of any change for the 50°C annealing can clearly be seen,

8

as can the effect of a smaller horizontal size after annealing at 90°C. However, the height of the objects increased.

The height increase is also visible in the images taken with the ESEM, which is shown in Figure 9. It is clear from the image that the calibration of the 3-D printer was not optimal, because while it was instructed to give the object solid infill, there are large air spaces present. The lines are also grouped in pairs, which suggests hysteresis in the machine that causes the lines that are printed while the nozzle is moving one way to be slightly offset from the lines that are printed while the nozzle is going the other direction.
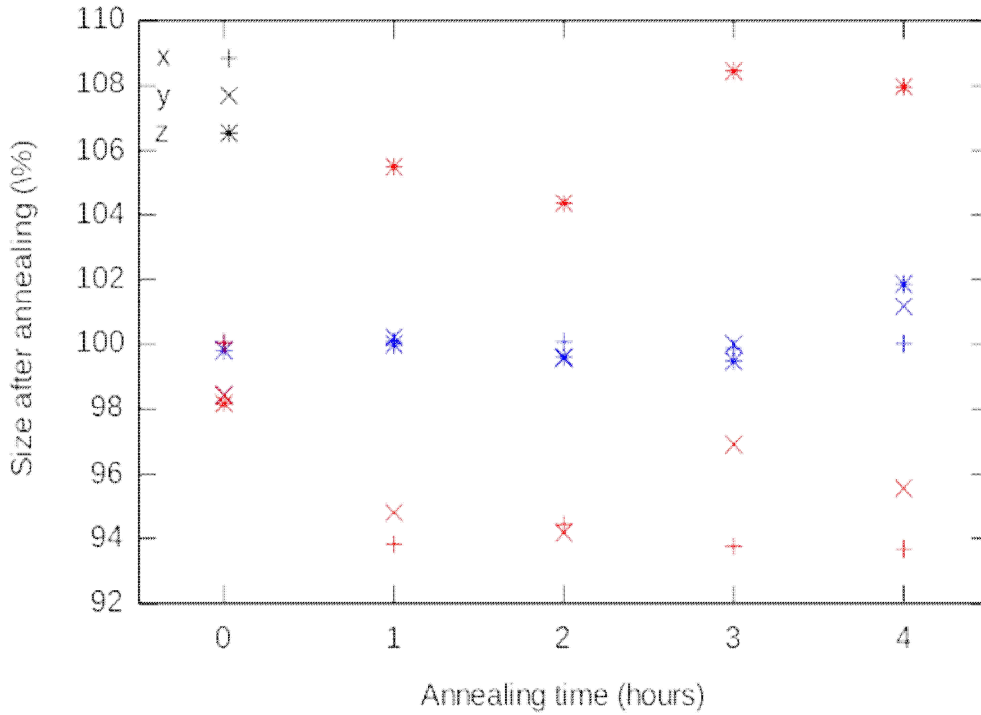

Figure 8: Changes in size after annealing at 50°C and 90°C. At 50°C (blue markers) there is no change in size, while at 90°C (red markers) the objects have shrunk horizontally, but grown vertically.

Figure 9: The surface of the fracture interface of 1 hour annealed (top) and unannealed (bottom) samples, taken with an Environmental Electron Scanning Microscope (ESEM).

Before annealing, the cross section of the printed filament is flattened, and after annealing it is more circular, as can be seen in Figure 9. The ratio between width and height, measured from the images, is 0.82 for the sample that was annealed at 90°C and 0.74 for the sample that was not (both with a standard deviation of 0.08).

The measurements on the warped vertical wall are shown in Figure 10. The curve is the prediction from the model, purely based on the thermal data. It is very close to the actual values given that the temperature fit had a sizable error and simplifications were made to the physics. The points at larger heights are expected to be closer to the curve, because the substrate is not part of the model and its effect is smaller at greater thicknesses. The method also expected the part to start warping while the head was on the last layer in the position as shown in Figure 4, but in practice it took a few seconds to break it off the substrate, so it had cooled a little more than what the model expected. Because of this, the values are expected to be slightly lower than what the model predicts.
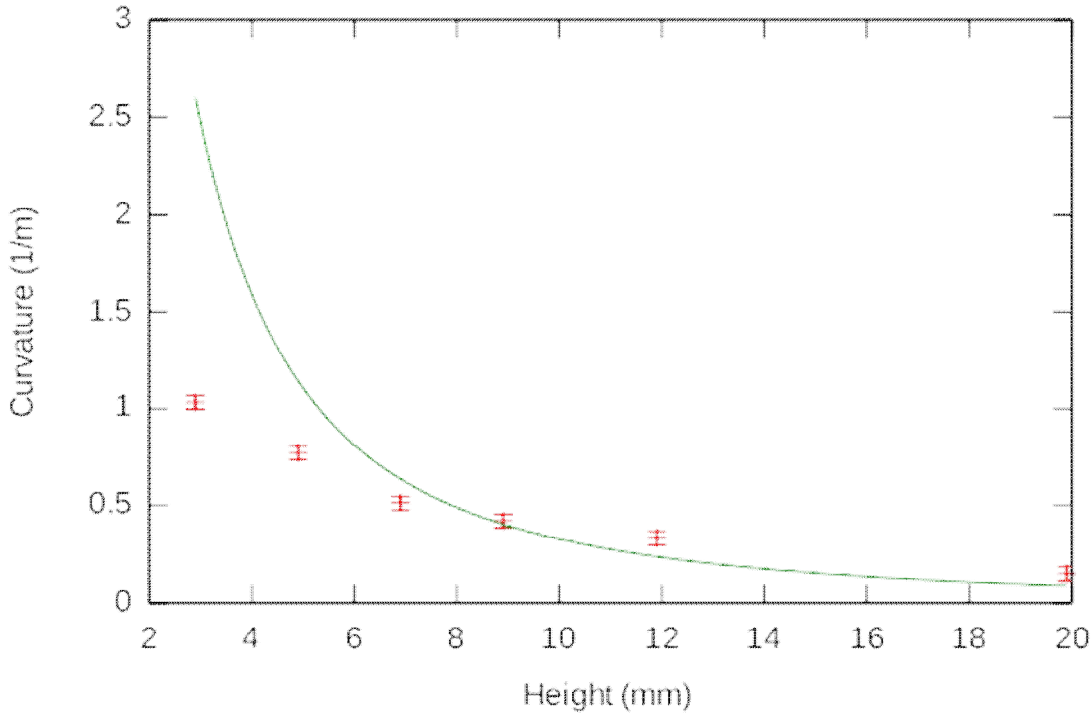

Figure 10: Measured warp and model predictions (equation 5). The curve is the model's prediction with the variables from the fit to the thermal graph.

5. Discussion

The thermal model presented here is based on physics and a real world temperature gradient. It is therefore more realistic than what was used by Wang et al. [49]. The model successfully predicts warpage of amorphous objects. The expectation is that it also works for other plastics, but that remains to be tested. The behavior of the curvature is correctly predicted, but the magnitude is too high, especially for lower print layers. This is likely caused by the simplifications in the model, such as ignoring the effects of the substrate. This has a larger effect on lower prints, so the larger error in the prediction was expected.

Some experiments were also done to show the effect of annealing on printed objects. This is especially relevant for printers with a heated substrate or chamber, because those printers are annealing the objects during the print. It was found that at a temperature of 50°C, which is just below the glass transition temperature of 58°C, the objects neither shrink nor crystallize, while at 90°C, they rapidly crystallize and shrink considerably. In order to draw conclusions about this effect, it must first be studied as a function of infill. Colored PLA already has some crystallinity as shipped [48]. Further study is required to see if this means that it shrinks less, or that it more readily crystallizes and reaches higher crystallinity, thus shrinking more. The crystallization explains why long prints can release from the substrate several hours into the print. This suggests that keeping the temperature of the substrate below 50°C would prevent this problem with natural PLA.

An unexpected effect of annealing was that the height of the objects increased. While there was a 5% size decrease in both horizontal dimensions, there was an 8% increase in the vertical dimension, so the average volume decrease per dimension is only 0.8%. Crystallization is expected to cause a volume decrease of 3.3%, so at 22% crystallinity that is only a 0.72% volume decrease, or 0.24% per dimension. The other 0.6% of shrinkage per dimension may be caused by relaxation of residual stress. An 8% increase in z means a shrinkage in x and y of 3% with Poisson's ratio $\nu = 0.36$. This is less than the observed 5% of shrinkage.

An alternative approach is to consider the shrinkage that would have occurred if the object were not held by the substrate. This is the shrinkage that would be expected as a result of complete stress relaxation, assuming that no relaxation has taken place while the object was constrained. The linear shrinkage coefficient is $8.5 \cdot 10^{-5}\,K^{-1}$, so for a temperature drop from 210°C at extrusion to 25°C, a shrinkage of 1.6% would be expected. This is far below the 3.0% that was derived above, so the increased height cannot be explained solely by horizontal stress relaxation.

The ESEM images show an additional effect, which can be responsible for a part of the height increase – the change is circularity of the printed filament show in Figure 9. This may be caused by the material decreasing its surface energy. The imaged parts show different deformation than the complete sample: 10.1% horizontal shrinkage, and 3.4% vertical expansion. The ratio in density can be determined from these numbers, by assuming that the view in the x and y directions is the same. Measuring the lengths of equal parts in both images and multiplying the horizontal length squared with the vertical length gives a volume. This volume has equal mass in both images, so the ratio of densities can be found by dividing them. This gives a ratio of 83.4%. According to the theory, amorphous PLLA is 1248 kg/m^3, while crystalline PLLA is 1290 kg/m^3. This is a ratio of 96.7%, and because the crystallinity is around 20%, not 100%, the ratio due to crystallinity in these samples is 99.3%.

Analyzing the images in Figure 9 using a pixel count in the GNU Image Manipulation Program, it was determined that the air content before annealing was 21.3%, while after annealing it was 21.5%. Given the magnitude of the changes in size, this can be safely ignored.

These results can also be used to better guide slicing routines for large objects printed in PLA or other polymers that build up internal stress. In Wang's article [49] a combination contour raster is chosen, which takes advantage of the good surface finish and dimensional accuracy of a contour on the outer layers, and then the high speed deposition of a raster on the interior. Such a method of separating fill and exterior is common in all open source slicing programs (e.g. Cura and Slic3r). [50] had proposed an alternative method for toolpath creation that has demonstrated less warpage of the printed object. It involves breaking up long runs into bricks. With the same curvature, this limits deformation by shortening the length of the curving pieces, but this comes at the cost of loss in strength. In addition, the actual toolpath that was used for bricking was not divulged. There are options in current slicing for making almost brick-like patterns. For example, a Hilbert curve can be used as the bottom fill pattern in Slic3r, which is a continuous brick like pattern. Future work is needed to determine if this continuous bricking is acceptable for specific applications and the optimal size of bricks, the shape (square or hexagonal), the stacking orientation, the toolpath within a brick (e.g. rastor vs contour or some combination and the level of infill) and the printing temperature.

Although this study successfully explained how the deformation of PLA is caused by the temperature gradient that builds up during the print, it did not investigate how to stop it. However, the results of this study indicate a potential solution. It involves using the model developed here, improving upon it by excluding the simplifications, and then using it to predict the exact deformation of a brick building block. Then an object must be sliced into bricks with space for mortar of the size needed to fill the expected deformation on a sealing pass. The mortar must be printed after the layer has cooled and shrunk, and would ideally be determined by the nozzle diameter of the FFF machine. Finally, the mortar tool path would need to be optimized to minimize single toolpath lengths while binding all he bricks into a single unit. Future work is necessary to test this new method of slicing to prevent fatal deformation of large-scale FFF, and how it affects the mechanical properties of the printed objects.

6. Conclusions

The deformation model presented by Wang et al. for chamber based FDM was generalized for FFF 3-D printing with a room temperature environment and expanded to use a physics based temperature gradient. The thermal equation was calibrated using thermal measurements and validated by measuring curvature in printed objects. The results showed that this makes the model usable for lower ambient temperatures. It is not very accurate for the first layers, but after about 9 mm it predicts the deformation well. Additionally, the effect of annealing was examined. It was found that at a temperature of 50°C, no shrinkage or crystallization takes place, but at 90°C the PLA rapidly crystallizes to around 20% crystallinity. This indicates that heated bed temperatures should be maintained at 50°C or lower to avoid delamination of the print from the substrate with PLA. At 90°C, the annealing is accompanied by a 5% size decrease in both horizontal dimensions, but an 8% increase in the vertical dimension. Thus, the volume decreased by 3%, indicating some potential slicing measures that could

reduce deformation of a printed object.

7. References

1. Sells E, Smith Z, Bailard S, Bowyer A, Olliver V (2010) RepRap: the replicating rapid prototyper: maximizing customizability by breeding the means of production. In: Piller FT, Tseng MM (ed) Handbook of Research in Mass Customization and Personalization, World Scientific, Singapore, pp 568-581
2. Jones R, Haufe P, Sells E, Iravani P, Olliver V, Palmer C, Bowyer A (2011) RepRap–the replicating rapid prototyper. *Robotica* 29(01):177-191. doi: 10.1017/S026357471000069X
3. Bowyer A (2014) 3D Printing and Humanity's First Imperfect Replicator. *3D printing and Additive Manufacturing* 1(1), 4-5. doi: 10.1089/3dp.2013.0003
4. RepRap Options (2017). http://reprap.org/wiki/RepRap_Options Accessed 3 January 2017
5. Wohlers T, Caffery T (2015) Wohlers Report 2015: Additive Manufacturing and 3D Printing State of the Industry: Annual Worldwide Progress Report. Wohlers Associates, Fort Collins, Colorado
6. Make. (2015) Here Are This Year's Winners from Make:'s Digital Fabrication Shootout. Make. http://makezine.com/2015/11/04/digital-fabrication-shootout-winners/ Accessed 3 January 2017
7. Priore, R. Make (2016) Prusa i3 MK2. http://makezine.com/product-review/prusa-i3-mk2/ Accessed 3 January 2017
8. Pearce JM, Blair CM, Laciak KJ, Andrews R, Nosrat A, Zelenika-Zovko I (2010) 3-D printing of open source appropriate technologies for self-directed sustainable development. *Journal of Sustainable Development* 4:17-29.
9. Gwamuri J, Franco D, Khan KY, Gauchia L, Pearce JM High-Efficiency Solar-Powered 3-D Printers for Sustainable Development. *Machines* 2016, 4(1), 3. doi: 10.3390/machines4010003
10. Canessa E, Fonda C, Zennaro M (2013) Low-cost 3D printing for science, education and sustainable development. *Low-Cost 3D Printing* 11.
11. Birtchnell T, Hoyle W (2014) 3D printing for development in the global south: The 3D4D challenge. Palgrave Macmillan.
12. Mota C (2011) The rise of personal fabrication. In Proceedings of the 8th ACM conference on Creativity and cognition, ACM, pp 279-288
13. Laplume A, Anzalone GC, Pearce JM (2016) Open-source, self-replicating 3-D printer factory for small-business manufacturing. *The International Journal of Advanced Manufacturing Technology*. 85(1): 633–642. doi:10.1007/s00170-015-7970-9
14. Pearce JM (2012) Building Research Equipment with Free, Open-Source Hardware *Science* 337 (6100):1303-1304. doi: 10.1126/science.1228183
15. Zhang C, Anzalone NC, Faria RP, Pearce JM (2013) Open-Source 3D-Printable Optics Equipment. *PLoS ONE* 8(3): e59840. doi:10.1371/journal.pone.0059840
16. Pearce JM (2014) *Open-Source Lab: How to Build Your Own Hardware and Reduce Research Costs*, Elsevier
17. Wijnen B, Hunt EJ, Anzalone GC, Pearce JM (2014) Open-source Syringe Pump Library. *PLoS ONE* 9(9): e107216. doi:10.1371/journal.pone.0107216
18. Wijnen B, Anzalone GC, Pearce JM (2014) Open-source mobile water quality testing platform. *Journal of Water, Sanitation and Hygiene for Development* 4(3): 532-537. doi:10.2166/washdev.2014.137
19. Lücking TH, Sambale F, Beutel S, Scheper T (2015) 3D printed individual labware in biosciences by rapid prototyping: A proof of principle. *Engineering in Life Sciences* 15(1): 51-56. doi: 10.1002/elsc.201400093
20. Gross BC, Erkal JL, Lockwood SY, Chen C, Spence DM (2014). Evaluation of 3d printing and its potential impact on biotechnology and the chemical sciences. *Analytical Chemistry* 86(7), 3240-3253. doi: 10.1021/ac403397r
21. Baden T, Chagas AM, Gage G, Marzullo T, Prieto-Godino LL, Euler T (2015). Open Labware: 3-D Printing Your Own Lab Equipment. *PLOS Biology* 13(3). doi: 10.1371/journal.pbio.1002086
22. Zhang C, Wijnen B, Pearce JM (2016) Open-source 3-D Platform for Low-cost Scientific Instrument Ecosystem. *Journal of Laboratory Automation*. 21(4): 517-525. doi: 10.1177/2211068215624406
23. Pearce JM, Anzalone NC, Heldt CL (2016) Open-source Wax RepRap 3-D Printer for Rapid Prototyping Paper-Based Microfluidics, *Journal of Laboratory Automation 21(4):510–516*. doi: 10.1177/2211068215624408
24. Wittbrodt BT, Pearce JM (2015) Total U.S. cost evaluation of low-weight tension-based photovoltaic flat-roof mounted racking. *Solar Energy* 117: 89–98. doi: 10.1016/j.solener.2015.04.026
25. Wittbrodt BT, Laureto J, Tymrak B, Pearce JM (2015) Distributed manufacturing with 3-D printing: a case study of recreational vehicle solar photovoltaic mounting systems. *Journal of Frugal Innovation* 1(1): 1-7. doi:10.1186/s40669-014-0001-z
26. Kasparova M, Grafova L, Dvorak P, Dostalova T, Prochazka A, Eliasova H, Prusa J, Kakawand S (2013) Possibility of reconstruction of dental plaster cast from 3D digital study models. *Biomed Eng Online*, *12*(49):1-11.

doi: 10.1186/1475-925X-12-49

27. Burde AV, Constantiniuc M, Câmpian RS (2015) Applications of RepRap three-dimensional printers in dentistry – a literature review. *International Journal of Medical Dentistry* 5(1):37-43.

28. Kuehn BM (2016) Clinicians Embrace 3D Printers to Solve Unique Clinical Challenges. *JAMA*, *315*(4):333-335. doi:10.1001/jama.2015.17705

29. Herrmann KH, Gärtner C, Güllmar D, Krämer M, Reichenbach JR (2014) 3D printing of MRI compatible components: Why every MRI research group should have a low-budget 3D printer. *Medical engineering & physics* 36(10):1373-1380. doi: 10.1016/j.medengphy.2014.06.008.

30. Niezen G, Eslambolchilar P, Thimbleby H (2016) Open-source hardware for medical devices. *BMJ Innovations* 2:78-83 doi:10.1136/bmjinnov-2015-000080

31. Chae MP, Rozen WM, McMenamin PG, Findlay MW, Spychal RT, Hunter-Smith DJ (2015) Emerging applications of bedside 3D printing in plastic surgery. *Frontiers in surgery*, *2*. doi: 10.3389/fsurg.2015.00025

32. Pearce, JM (2015) Applications of Open Source 3-D Printing on Small Farms. *Organic Farming* 1(1), 19-35. doi: 10.12924/of2014.01010019

33. Grujović N, Radović M, Kanjevac V, Borota J, Grujović G, Divac D (2011) 3D printing technology in education environment. In *34th International Conference on Production Engineering,* pp 29-30

34. Kentzer J, Koch B, Thiim M, Jones RW, Villumsen E (2011) An open source hardware-based mechatronics project: The replicating rapid 3-D printer. In *Mechatronics (ICOM), 2011 4th International Conference On.* IEEE, pp. 1-8

35. Irwin JL, Pearce JM, Anzolone GC, Oppliger DE (2014) The RepRap 3-D printer revolution in STEM education. In *121st ASEE Annual Conference & Exposition.*

36. Gonzalez-Gomez J, Valero-Gomez A, Prieto-Moreno A, Abderrahim M (2012) A new open source 3d-printable mobile robotic platform for education. In *Advances in autonomous mini robots.* Springer Berlin Heidelberg, pp. 49-62.

37. Schelly C, Anzalone GC, Wijnen B, Pearce JM (2015) Open-source 3-D printing technologies for education: Bringing additive manufacturing to the classroom. *Journal of Visual Languages & Computing* 28:226-237. doi: 10.1016/j.jvlc.2015.01.004

38. Szulżyk-Cieplak J, Duda A, Sidor B (2014) 3D printers–new possibilities in education. *Advances in Science and Technology Research Journal* 8(24)

39. Horowitz SS, Schultz PH (2014) Printing space: Using 3D printing of digital terrain models in geosciences education and research. *Journal of Geoscience Education* 62(1):138-145

40. Short DB (2015) Use of 3D Printing by Museums: Educational Exhibits, Artifact Education, and Artifact Restoration. *3D Printing and Additive Manufacturing* 2(4):209-215. doi:10.1089/3dp.2015.0030.

41. Omnexus (2017) Thermal expansion: http://omnexus.specialchem.com/polymer-properties/properties/coefficient-of-linear-thermal-expansion Accessed 3 January 2017

42. Stephens B, Azimi P, El Orch Z, Ramos T (2013) Ultrafine particle emissions from desktop 3D printers. *Atmospheric Environment* 79:334-9. doi:10.1016/j.atmosenv.2013.06.050

43. Sin LT, Rahmat AR, Rahman WAWA. *Polylactic acid: PLA biopolymer technology and applications*. William Andrew, 2012.

44. Natureworks ingeo (2017) http://www.natureworksllc.com/The-Ingeo-Journey Accessed 3 January 2017

45. https://re3d.org Accessed 3 January 2017

46. Kochan D, Kai CC, Zhaohui D (1999) Rapid prototyping issues in the 21st century. Comput Ind 39(1):3–10. doi: 10.1016/S0166-3615(98)00125-0

47. Mercelis P, Kruth JP (2006) Residual stresses in selective laser sintering and selective laser melting *Rapid Prototyping Journal* 12(5):254-265. doi:10.1108/13552540610707013

48. Wittbrodt B, Pearce JM (2015) The effects of PLA color on material properties of 3-d printed components *Additive Manufacturing* 8:110-116.doi: 10.1016/j.addma.2015.09.006

49. Wang TM, Xi JT, Jin Y (2007) A model research for prototype warp deformation in the FDM process. *The International Journal of Advanced Manufacturing Technology* 33(11-12):1087-1096. doi: 10.1007/s00170-006-0556-9

50. Guerrero-de Mier A, Espinosa M, Domínguez M (2015) Bricking: A new slicing method to reduce warping *Procedia Engineering* 132:126-131. doi: 10.1016/j.proeng.2015.12.488

51. Xinhua L, Shengpeng L, Zhou L, Xianhua Z, Xiaohu C, Zhongbin W (2015) An investigation on distortion of pla thin-plate part in the fdm process. *The International Journal of Advanced Manufacturing Technology* 79(5-8):1117-1126. doi: 10.1007/s00170-015-6893-9

52. Long S, Atluri SN (2002) A Meshless Local Petrov-Galerkin Method for Solving the Bending Problem of a Thin Plate *Computer modeling in engineering & sciences* 3(1):53-63. doi:10.3970/cmes.2002.003.053

53. Garlotta D (2001) A literature review of poly (lactic acid) *Journal of Polymers and the Environment* 9:63-84. doi: 10.1023/A:1020200822435
54. Saeidlou S, Huneault MA, Li H, Park CB (2012) Poly(lactic acid) crystallization *Progress in Polymer Science* 37:1657-1677.
55. Henton DE, Gruber P, Lunt J, Randall J (2005) Polylactic acid technology *Natural fibers, biopolymers, and biocomposites.* 16:527-577
56. Wu S (1982) Polymer interface and adhesion. Marcel Dekker, New York
57. Payne T (2017) Heated Build Chamber for Rapman 3D Printer. *Instructables.* http://www.instructables.com/id/Heated-Build-Chamber-for-Rapman-3D-Printer/ Accessed 3 January 2017
58. Repkid (2017) Heated Build Chamber. http://reprap.org/wiki/Heated_Build_Chamber Accessed 3 January 2017
59. Yru. (2017) GolemD. RepRap wiki. http://reprap.org/wiki/GolemD Accessed 3 January 2017
60. 3Ders. (2017) Introducing Kühling&Kühling RepRap industrial 3D printer. 3Ders. http://www.3ders.org/articles/20130220-introducing-kuhling-kuhling-reprap-industrial-3d-printer.html Accessed 3 January 2017
61. Carrasco F, Pagès P, Gámez-Pérez J, Santana O, Maspoch ML (2010) Processing of poly (lactic acid): characterization of chemical structure, thermal stability and mechanical properties. *Polymer Degradation and Stability* 95(2):116-125
62. Natureworks (2017) 4043D polylactide acid http://www.natureworksllc.com/Product-and-Applications/3D-Printing Accessed 3 January 2017
63. Anzalone, G.C., Wijnen, B. and Pearce, J.M., 2015. Multi-material additive and subtractive prosumer digital fabrication with a free and open-source convertible delta RepRap 3-D printer. *Rapid Prototyping Journal*, *21*(5), pp.506-519.
64. Wijnen B, Anzalone GC, Haselhuhn AS, Sanders PG, Pearce JM (2016) Free and open-source control software for 3-D motion and processing *Journal of Open Research Software* 4(1)
65. Franklin (2017) Github. https://github.com/mtu-most/franklin Accessed 3 January 2017
66. OpenSCAD (2017) 2015.03-1 http://www.openscad.org Accessed 3 January 2017
67. Slic3r (2017) 1.2.9 http://www.slic3r.org Accessed 3 January 2017
68. OSF. (2017) https://osf.io/4kvwm/ Accessed 3 January 2017
69. GNU Image Manipulation Program (2017) 2.8.16, http://www.gimp.org Accessed 3 January 2017